Protease activity sensors enable real-time treatment response monitoring in lymphangioleiomyomatosis

Protease activity sensors enable real-time treatment response monitoring in lymphangioleiomyomatosis

Jesse D. Kirkpatrick[1,2], Ava P. Soleimany[1,2,3,4], Jaideep S. Dudani[1,5], Heng-Jia Liu[6], Hilaire C. Lam[6], Carmen Priolo[6], Elizabeth P. Henske[6,12] and Sangeeta N. Bhatia[1,2,7,8,9,10,11,12]

[1]Koch Institute for Integrative Cancer Research, Massachusetts Institute of Technology, Cambridge, MA, USA. [2]Harvard-MIT Division of Health Sciences and Technology, Institute for Medical Engineering and Science, Massachusetts Institute of Technology, Cambridge, MA, USA. [3]Harvard Graduate Program in Biophysics, Harvard University, Boston, MA, USA. [4]Microsoft Research New England, Cambridge, MA, USA. [5]Dept of Biological Engineering, Massachusetts Institute of Technology, Cambridge, MA, USA. [6]Pulmonary and Critical Care Medicine, Dept of Medicine, Brigham and Women's Hospital and Harvard Medical School, Boston, MA, USA. [7]Howard Hughes Medical Institute, Cambridge, MA, USA. [8]Dept of Electrical Engineering and Computer Science, Massachusetts Institute of Technology, Cambridge, MA, USA. [9]Dept of Medicine, Brigham and Women's Hospital, Harvard Medical School, Boston, MA, USA. [10]Broad Institute of Massachusetts Institute of Technology and Harvard, Cambridge, MA, USA. [11]Wyss Institute at Harvard, Boston, MA, USA. [12]E.P. Henske and S.N. Bhatia co-supervised the study.

Corresponding author: Sangeeta N. Bhatia (sbhatia@mit.edu)

Shareable abstract (@ERSpublications)
Nanoparticles that noninvasively measure the activity of proteases in the lungs enable real-time monitoring of disease progression and therapeutic response in a mouse model of lymphangioleiomyomatosis https://bit.ly/3z4cnAh

Cite this article as: Kirkpatrick JD, Soleimany AP, Dudani JS, *et al*. Protease activity sensors enable real-time treatment response monitoring in lymphangioleiomyomatosis. *Eur Respir J* 2022; 59: 2100664 [DOI: 10.1183/13993003.00664-2021].

This article has an editorial commentary: https://doi.org/10.1183/13993003.00405-2022

Received: 4 March 2021
Accepted: 14 Aug 2021

Abstract

Background Biomarkers of disease progression and treatment response are urgently needed for patients with lymphangioleiomyomatosis (LAM). Activity-based nanosensors, an emerging biosensor class, detect dysregulated proteases *in vivo* and release a reporter to provide a urinary readout of disease. Because proteases are dysregulated in LAM and may directly contribute to lung function decline, activity-based nanosensors may enable quantitative, real-time monitoring of LAM progression and treatment response. We aimed to assess the diagnostic utility of activity-based nanosensors in a pre-clinical model of pulmonary LAM.

Methods *Tsc2*-null cells were injected intravenously into female nude mice to establish a mouse model of pulmonary LAM. A library of 14 activity-based nanosensors, designed to detect proteases across multiple catalytic classes, was administered into the lungs of LAM mice and healthy controls, urine was collected, and mass spectrometry was performed to measure nanosensor cleavage products. Mice were then treated with rapamycin and monitored with activity-based nanosensors. Machine learning was performed to distinguish diseased from healthy and treated from untreated mice.

Results Multiple activity-based nanosensors (PP03 (cleaved by metallo, aspartic and cysteine proteases), $p_{adjusted}<0.0001$; PP10 (cleaved by serine, aspartic and cysteine proteases), $p_{adjusted}=0.017$)) were differentially cleaved in diseased and healthy lungs, enabling strong classification with a machine learning model (area under the curve (AUC) 0.95 from healthy). Within 2 days after rapamycin initiation, we observed normalisation of PP03 and PP10 cleavage, and machine learning enabled accurate classification of treatment response (AUC 0.94 from untreated).

Conclusions Activity-based nanosensors enable noninvasive, real-time monitoring of disease burden and treatment response in a pre-clinical model of LAM.

Introduction

Lymphangioleiomyomatosis (LAM) is a rare lung disorder that is characterised by cystic lung destruction, progressive lung function decline and lung failure [1]. Pathologically, LAM is characterised by abnormal proliferation of smooth muscle-like LAM cells in the lung that may originate from the uterus [2]. LAM cells have biallelic loss-of-function mutations in tuberous sclerosis complex (TSC) 1 or 2, which act to

inhibit the mechanistic target of rapamycin complex 1 (mTORC1). LAM cells aberrantly express proteases (predominantly matrix metalloproteinase (MMP) 2 and 9 [3–5] and cathepsin K (CTSK)), which have collagenolytic activity [6] and may contribute directly to lung degradation and cyst formation [7–9]. Consistent with the role of mTORC1 in this disease process, rapamycin is the standard of care for patients with LAM [10, 11]. However, rapamycin treatment is not curative and the disease progresses when treatment is discontinued, requiring continuous therapy with associated side-effects [11, 12]. Currently, pulmonary function tests, including forced expiratory volume in 1 s (FEV_1), are the standard method of monitoring disease burden and response to therapy [13]. However, FEV_1 is prone to technical variability [14] and is slow to respond to therapy, hindering clinical decision making and impeding the pace of clinical trials. Therefore, quantitative, accurate and rapidly responsive biomarkers are urgently needed to monitor patients with LAM and evaluate the efficacy of novel therapies.

Given the limitations of existing biomarkers for LAM, various additional blood biomarkers and imaging tools have been explored [15]. Serum vascular endothelial growth factor (VEGF)-D is increased in the majority of patients with LAM [16, 17] and has thus been proposed as a candidate biomarker. However, VEGF-D has suboptimal sensitivity for LAM [17] and its levels do not reliably predict response to therapy [16]. A recent study revealed 32 circulating biomarkers, including VEGF-D, that changed significantly in the serum of LAM patients treated with a combination of rapamycin and hydroxychloroquine [18]. However, no analyte changes by week 3 of treatment were found to correlate with FEV_1 changes over the 24-week study duration. Finally, high-resolution computed tomography (HRCT) has been investigated as a candidate tool for monitoring therapeutic response, but imaging findings have not been shown to change in response to rapamycin treatment [19].

Because dysregulated proteases are a hallmark of LAM, we hypothesised that measuring protease activity could enable accurate and quantitative monitoring of disease. Our group has previously developed "activity-based nanosensors", which measure disease activity *in vivo* by querying protease activity at the site of disease [20–26]. Short, 8–12-amino-acid peptide substrates are conjugated to a nanoparticle and administered intravenously or intratracheally. At the disease site, peptide substrates are cleaved by dysregulated proteases, liberating barcoded "reporters" that are cleared into the urine, where they can be detected by mass spectrometry (MS). By appending each substrate with a unique reporter, multiple substrates can be tested simultaneously. Here, we establish the utility of activity-based nanosensors in a novel mouse model of pulmonary LAM. Using machine learning, we build classifiers that accurately read out LAM disease activity and progression, and rapidly detect response to rapamycin therapy. Collectively, these results support the clinical development of activity-based nanosensors for monitoring progression and treatment response in LAM.

Methods

Additional details are provided in the supplementary material.

Animal experiments

All animal studies were approved by the Committee on Animal Care of Massachusetts Institute of Technology (Cambridge, MA, USA) (protocol 0420-023-23). For all procedures requiring anaesthesia, mice were anesthetised by isoflurane (Zoetis, Parsippany, NJ, USA) inhalation.

Mouse model of pulmonary LAM

105K cells were transduced with a lentivirus encoding for luciferase and a puromycin selection cassette (LP-hLUC-Lv201-0200; Genecopoeia, Rockville, MD, USA), followed by selection with puromycin ($1\ \mu g \cdot mL^{-1}$). To establish an *in vivo* LAM model, female nude mice (3–4 weeks old) were injected *i.v.* with 5×10^5 luciferised 105K cells (105K-Luc). Disease burden was monitored by the IVIS *in vivo* imaging system (PerkinElmer, Waltham, MA, USA). For *in vivo* administration, rapamycin was prepared in a vehicle containing 0.25% poly(ethylene glycol) (PEG)-200 and 0.25% Tween-80. LAM mice were treated with intraperitoneal injections of rapamycin (LC Laboratories, Woburn, MA, USA) (1 or $3\ mg \cdot kg^{-1}$) or vehicle 3–4 times per week and were monitored by the IVIS system.

In vivo *disease monitoring with activity-based nanosensors*

Nanosensors (Glu-Fib–substrate–PEG-$8_{40\ kDa}$) for urinary experiments were synthesised by CPC Scientific (San Jose, CA, USA) and sterile filtered with 0.2 µm syringe filters prior to use. Nanosensors were dosed (50 µL total volume, 20 µM concentration per nanosensor) in mannitol buffer (0.28 M mannitol, 5 mM sodium phosphate monobasic, 15 mM sodium phosphate dibasic, pH 7.0–7.5) by *i.t.* instillation, immediately followed by a subcutaneous injection of PBS (200 µL) to increase urine production. Bladders were voided 60 min after nanosensor administration and all urine produced 60–120 min after administration

was collected. Urine from each mouse was pooled and frozen at −80°C. Liquid chromatography (LC)-MS/MS was performed as described previously [21].

Statistical analysis

For all urine experiments, urinary peak area ratio (PAR) values generated by LC-MS/MS were normalised to the PAR of each nanosensor in the injected dose and then mean-scaled across all reporters in a given urine sample before further statistical analysis. To identify differential urinary reporters, all reporters were analysed by unpaired two-tailed t-tests, followed by correction for multiple hypotheses using the Holm–Šídák method in Prism version 7.0 (GraphPad, San Diego, CA, USA). $p_{adjusted}<0.05$ was considered significant. Principal component analysis (PCA) was performed on mean-scaled PAR values and implemented in R using the prcomp package and visualised using ggplot2 (www.r-project.org). For disease classification based on urinary activity-based nanosensor signatures, randomly assigned sets of paired data samples consisting of features (the mean-scaled PAR values) and labels (*e.g.* "LAM (18 days)" and "Rap (+2 days)") were used to train random forest classifiers implemented with the TreeBagger class in MATLAB R2019b (www.mathworks.com). Estimates of out-of-bag error were used for cross-validation and trained classifiers were tested on randomly assigned, held-out test cohorts. 10 independent train–test trials were run for each classification problem and classification performance was evaluated with receiver operating characteristic statistics calculated in MATLAB. Classifier performance was reported as the mean accuracy and the area under the curve (AUC) across the 10 independent trials.

Results

Tsc2 *deficiency induces protease dysregulation*

We first sought to establish a mouse model that captured the dysregulated protease activity that is characteristic of LAM [1]. We leveraged a *Tsc2*-null kidney cystadenoma cell line, termed "105K", that was previously derived from a renal tumour that spontaneously formed in a $Tsc2^{+/-}$ mouse [27]. Analysis of spontaneous mouse kidney cystadenomas similar to those used to isolate the 105K cells revealed punctate expression of MMP2 and MMP9 and intense, ubiquitous expression of CTSK (figure 1a, top). All three proteases were absent in wild-type mouse kidneys (figure 1a, bottom). Consistent with reports that LAM-associated CTSK activity is dependent on an acidic micro-environment [28], Western blot of lysates from 105K cells cultured at neutral pH revealed a 37 kDa band corresponding to pro-CTSK [29] (figure 1b). A 27 kDa band, consistent with the size of the active protease form, was detected when recombinantly expressed mouse CTSK protein was run on the same gel. No anti-CTSK-reactive bands were observed in wild-type mouse kidney or lung homogenates (figure 1b). Finally, we found that 105K cells secreted multiple metalloproteases *in vitro*, and that expression levels of MMP2, MMP3, MMP8 and MMP12 were significantly abrogated by re-introduction of *Tsc2* (figure 1c).

Tsc2-*null cells are responsive to rapamycin* in vitro *and* in vivo

The *Tsc1* and *Tsc2* genes encode hamartin and tuberin, respectively, which form a complex to inhibit the mTORC1 cascade [10, 30]. Loss of either hamartin or tuberin results in deregulation of mTOR signalling, and thus uncontrolled cell growth and proliferation. We sought to assess whether rapamycin, an mTOR inhibitor and the first-line therapy in patients with LAM, would inhibit 105K cell growth.

We first treated 105K cells with rapamycin *in vitro* and found that their growth was slowed in a dose-dependent manner (supplementary figure S1a). Next, we sought to assess whether 105K cells could be introduced into the lungs of mice to induce disease resembling human LAM. Previous models of LAM have leveraged *Tsc2*-null "TTJ" cells that were passaged as flank tumours to increase aggressiveness, but it was unknown whether the parental "105K" cells would efficiently seed the lungs [9]. To enable *in vivo* tracking of disease burden, we performed lentiviral transduction of 105K cells with a luciferase expression cassette. We then performed tail vein injection of 5×10^5 luciferase$^+$ 105K (105K-Luc) cells in nude mice and monitored luciferase expression by the IVIS system. We found that 105K-Luc cells seeded the lungs and formed detectable disease burden within 3 weeks post-inoculation, as assessed by the IVIS system (supplementary figure S1b, top) and histological assessment (supplementary figure S2). These lesions were proliferative, as evidenced by pronounced Ki-67 staining across all lesions (supplementary figure S3). To assess the efficacy of rapamycin *in vivo*, we treated mice with rapamycin either immediately after 105K-Luc cell inoculation ("Prevention") or 20 days after inoculation ("Treatment"). We observed very minimal disease in mice treated with rapamycin at day 0 and almost complete regression of disease within 8 days in mice treated at day 20 (supplementary figures S1b and c and S2).

Tsc2-*deficient lesions harbour aberrant protease activity*

We next sought to investigate protease activity in *Tsc2*-deficient lesions. We first injected 1×10^6 105K cells *s.c.* into the flanks of female nude mice and excised tumours when they reached volumes of

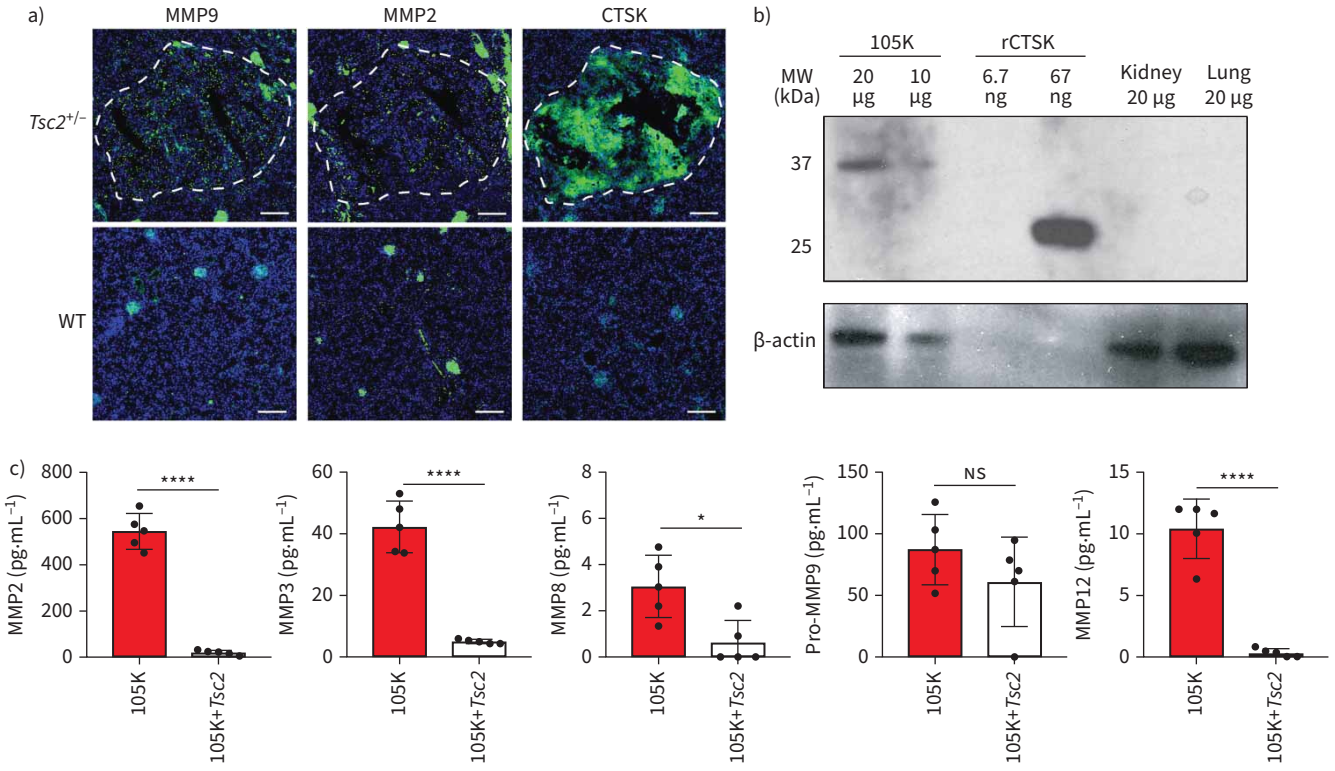

FIGURE 1 *Tsc2* deficiency results in aberrant protease expression. a) Immunofluorescence staining (green) of matrix metalloproteinases (MMP) 9 and 2 and cathepsin K (CTSK) in representative primary lesions (outlined in white) that formed spontaneously in the kidneys of *Tsc2*$^{+/-}$ mice (top) compared with kidneys from healthy control mice (bottom). Blue: 4′,6-diamidino-2-phenylindole (nuclei). Scale bars: 200 µm. b) Western blot against mouse CTSK in 105K cell lysates, recombinant mouse CTSK (rCTSK), and healthy mouse kidney and lung. β-actin immunostaining is shown for each sample. Quantity of protein loaded into each lane is noted. c) Expression (mean±SD), by multiplexed protein assay, of MMPs in conditioned media from 105K cells and 105K cells with retroviral re-introduction of *Tsc2* (n=5). NS: nonsignificant; *: p<0.05; ****: p<0.0001 by the two-tailed t-test. WT: wild-type; MW: molecular weight.

~500 mm^3. We incubated homogenates of these tumours, as well as lungs from healthy nude mice, with a panel of 16 quenched fluorescent protease substrates expected to be broadly cleaved by metallo, serine and cysteine proteases, and monitored fluorescence over time (supplementary figure S4a) [22, 24]. We found that multiple substrates were preferentially cleaved by *Tsc2*-deficient tumour homogenates relative to healthy lung (supplementary figure S4b). By subjecting the cleavage data to PCA, we found that 105K cleavage profiles clustered independently from healthy lungs, demonstrating global differences in proteolytic landscapes (supplementary figure S4c). To assess whether these proteolytic differences were preserved when 105K lesions were established in the lungs, we initiated the pulmonary LAM model *via i.v.* injection of 5×10^5 105K-Luc cells and collected bronchoalveolar lavage fluid (BALF) 5, 13 and 19 days later. We incubated BALF from diseased mice at 13 and 19 days, as well as healthy controls, with an additional panel of 16 quenched fluorescent substrates (supplementary figure S4d) and found, by PCA, global differences in pulmonary protease activity in diseased and healthy mice that increased with disease progression (supplementary figure S4e). Intriguingly, this study revealed that proteases in both BALF and homogenates from our LAM mouse models preferentially cleaved the substrates PP05 and PQ16, suggesting conservation of protease activity patterns in TSC2-deficient biospecimens regardless of the micro-environment (*i.e.* flank tumours *versus* pulmonary lesions) (supplementary figure S4b and d).

We then performed ELISA in BALF to quantify MMP9 and MMP2 concentrations in the lungs of mice with 105K lesions. We observed a striking increase in MMP9 concentration in the BALF of diseased mice 13 (p=0.0028) and 19 (p=0.0011) days after 105K cell inoculation (supplementary figure S5a). Furthermore, we found that MMP9 concentration correlated with disease burden, as assessed by the IVIS system (r^2=0.63, p=0.0007) (supplementary figure S5b). We observed a trend toward increased MMP2 concentration in BALF of diseased mice at day 19 (p=0.16) (supplementary figure S5c) and found that MMP2 concentration correlated with disease burden (r^2=0.49, p=0.0053) (supplementary figure S5d).

Immunofluorescence staining revealed ubiquitous CTSK expression in 105K lesions at day 19 (supplementary figure S6).

Activity-based nanosensors are efficiently cleaved by proteases across catalytic classes

Having established a mouse model of LAM, assessed its responsiveness to rapamycin and characterised its proteolytic landscape, we next sought to develop activity-based nanosensors tuned to detect these proteases. Because LAM is characterised by broad protease dysregulation, which was recapitulated in our mouse model, we selected a panel of 14 peptide substrates that we had previously found to be cleavable by proteases across multiple classes, including MMPs and cathepsins [21]. We first sought to characterise the sensitivity of each substrate for proteases of different catalytic classes. We synthesised quenched fluorescent versions of each substrate, designed such that fluorescence was activated upon proteolytic cleavage. We incubated each probe against a recombinant human metalloprotease (MMP2), serine protease (serine protease 3 (PRSS3)), aspartic protease (napsin A aspartic peptidase (NAPSA)) and cysteine protease (CTSK) at protease concentrations ranging from 10 pM to 10 nM and monitored fluorescence increase over time (supplementary figure S7). We found that each probe in the panel had a unique cleavage signature (supplementary figures S7 and S8) and that each protease was able to cleave at least one probe, with minimum detectable protease concentrations as low as 10 pM after 1 h of incubation (supplementary figure S8 and supplementary table S1). Thus, we concluded that the 14 nominated peptide substrates provided broad and sensitive coverage of proteases across catalytic classes.

PP03 is cleaved by aspartic proteases in Tsc2-deficient lesions under acidic conditions

We next sought to investigate the activity of different classes of proteases in *Tsc2*-deficient tissue and assess the ability of the 14 peptide substrates to detect each protease class. We diluted homogenates of *Tsc2*-deficient 105K cell flank tumours in pH 7.5 buffer and incubated them with each of the 14 fluorogenic peptide substrates, with or without inhibitors of metalloproteases (marimastat), serine proteases (4-(2-aminoethyl)benzenesulfonyl fluoride hydrochloride (AEBSF)), cysteine proteases (E64) and aspartic proteases (pepstatin). We found that only marimastat and AEBSF resulted in appreciable abrogation of peptide cleavage, suggesting that only metalloproteases and serine proteases were active in *Tsc2*-deficient tissue under neutral pH conditions (supplementary figure S9). Given recent reports of extracellular acidification driving pathological protease activity in LAM [28], we repeated this experiment in acidic (pH 5.25) buffer. Whereas the cleavage of 13 of the 14 peptides significantly decreased at acidic pH, the cleavage of one peptide, PP03, significantly increased ($p_{adjusted}$=0.011) (figure 2a). We therefore hypothesised that PP03 may be cleaved by either aspartic or cysteine proteases, which exhibit optimal activity under acidic conditions, in *Tsc2*-deficient tissue. We found that cleavage of PP03 was almost fully abrogated by the aspartic protease inhibitor pepstatin at pH 5.25 (p=0.0017) (figure 2b), but was unaffected by inhibitors against serine, metallo or cysteine proteases (figure 2c and d). In line with these observations, we found that PP03 was the peptide cleaved most efficiently by the aspartic protease NAPSA in our study (figure 2e). Collectively, these data suggest that the set of 14 substrates broadly detects metallo and serine proteases at neutral pH and PP03 specifically detects aspartic proteases at acidic pH in 105K tumour homogenates.

Activity-based nanosensors enable noninvasive detection of pulmonary 105K lesions in mice

To enable multiplexed protease activity measurement *in vivo*, each of these 14 substrates was uniquely labelled with a mass-encoded urinary reporter. As previously described [20], we used variable labelling of the 14-mer glutamate-fibrinopeptide B (Glu-Fib) with stable isotope-enriched amino acids to uniquely barcode each of the 14 peptide substrates. Multiple reaction monitoring *via* a liquid chromatography triple quadrupole mass spectrometer (LC-MS/MS) enabled quantitative assessment of urinary reporter concentration within a broad linear range [21]. Finally, these 14 barcoded protease substrates were conjugated to 40 kDa eight-arm PEG nanoparticles, as previously described [21].

We then performed *i.v.* injection of 5×10^5 105K-Luc cells and monitored disease development by the IVIS system (supplementary figure S10). We administered the 14-plex nanosensor panel by *i.t.* instillation in LAM mice 14 and 18 days after disease induction (figure 3a). All urine produced between 1 and 2 h after nanoparticle administration was collected and MS was performed. At 14 days, we observed significantly increased pulmonary protease activity against PP03, which we had previously found to be cleaved by aspartic proteases at low pH (figure 2), in LAM mice relative to healthy controls ($p_{adjusted}$=0.034) (figure 3b, left). Furthermore, among LAM mice at 14 days, PP03 signal was found to positively correlate (r=0.5871, p=0.0082) (supplementary figure S11a) with disease burden, and two sensors cleaved primarily by serine proteases [21], PP08 (r=−0.6983, p=0.0009) (supplementary figure S11b) and PP11 (r=−0.4617, p=0.0466) (supplementary figure S11c), negatively correlated with disease. Consistent with this finding, at 18 days, cleavage of PP03 was further increased in LAM mice ($p_{adjusted}=1.4\times10^{-5}$), and cleavage of PP08

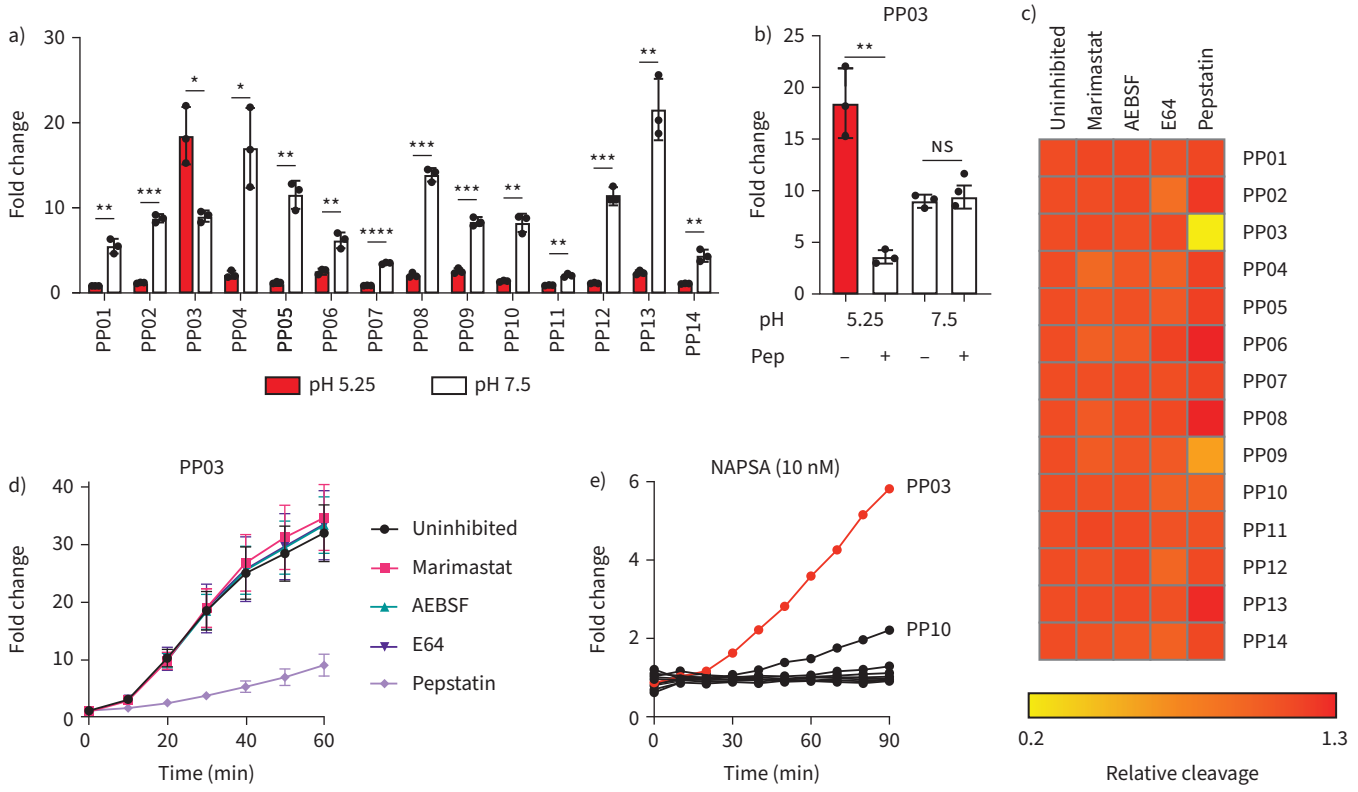

FIGURE 2 PP03 is cleaved by aspartic proteases in *Tsc2*-deficient lesions at acidic pH. a) Fluorescence fold change of PP01–PP14 after 30 min of incubation with 105K tumour homogenates diluted in pH 5.25 or pH 7.5 buffer. *: $p_{adjusted}$<0.05; **: $p_{adjusted}$<0.01; ***: $p_{adjusted}$<0.001; ****: $p_{adjusted}$<0.0001 by two-tailed t-test followed by adjustment for multiple hypotheses with Holm–Šídák correction. b) Fluorescence fold change of PP03 after 30 min of incubation with homogenates diluted in pH 5.25 or pH 7.5 buffer with or without pepstatin ("Pep"). NS: nonsignificant; **: p<0.01. c) Substrate cleavage after 30 min in homogenates diluted in pH 5.25 buffer incubated with or without inhibitors against metalloproteases (marimastat), serine proteases (4-(2-aminoethyl)benzenesulfonyl fluoride hydrochloride (AEBSF)), cysteine proteases (E64) or aspartic proteases (pepstatin), relative to uninhibited homogenates. d) Fluorescence increase over time of PP03 incubated with homogenates of 105K cell tumours at pH 5.25 with or without protease inhibitors. e) Fluorescence increase over time of PP01–PP14 incubated with napsin A aspartic peptidase (NAPSA). PP03 is shown in red.

($p_{adjusted}$=0.0047) and PP11 ($p_{adjusted}$=0.026) was significantly decreased (figure 3b, right). On the basis of these differentially cleaved nanosensors, we observed separation of LAM and healthy mice by unsupervised dimensionality reduction with PCA at both tested time-points (figure 3c). We then trained a random forest machine learning classifier using a subset of LAM mice and healthy controls from both time-points, and tested its ability to accurately classify mice in an independent, held-out cohort from the same experiment. We found that the classifier distinguished LAM mice from healthy controls as early as day 14 (AUC 0.81) and that classification was enhanced at 18 days (AUC 0.95) (figure 3d). Our results suggest that activity-based nanosensors can measure disease-associated protease dysregulation in a mouse model of pulmonary LAM, enabling accurate disease detection.

Activity-based nanosensors enable rapid treatment response evaluation in LAM mice

We then sought to assess whether activity-based nanosensors could enable objective, quantitative and rapid assessment of treatment response in LAM. We began treating LAM mice with rapamycin 18 days after disease induction and monitored their pulmonary protease activity with activity-based nanosensors at 2 and 8 days after rapamycin induction. Using the IVIS system, we observed a significant reduction in lung disease burden as early as 2 days after treatment initiation (p<0.0001), which further decreased after 8 days (supplementary figure S10b). We found that both sensors whose signal was significantly increased in LAM mice at 18 days, PP03 and PP10, returned to baseline within 2 days after treatment induction ($p_{adjusted}$=nonsignificant from control) (figure 4a). Notably, we also observed a transient increase above baseline in cleavage of PP04 ($p_{adjusted}$=0.0012 from control) and PP13 ($p_{adjusted}$=0.0042 from control) after rapamycin treatment (figure 4a). Overall, the cleavage of nine out of 14 nanosensors was significantly

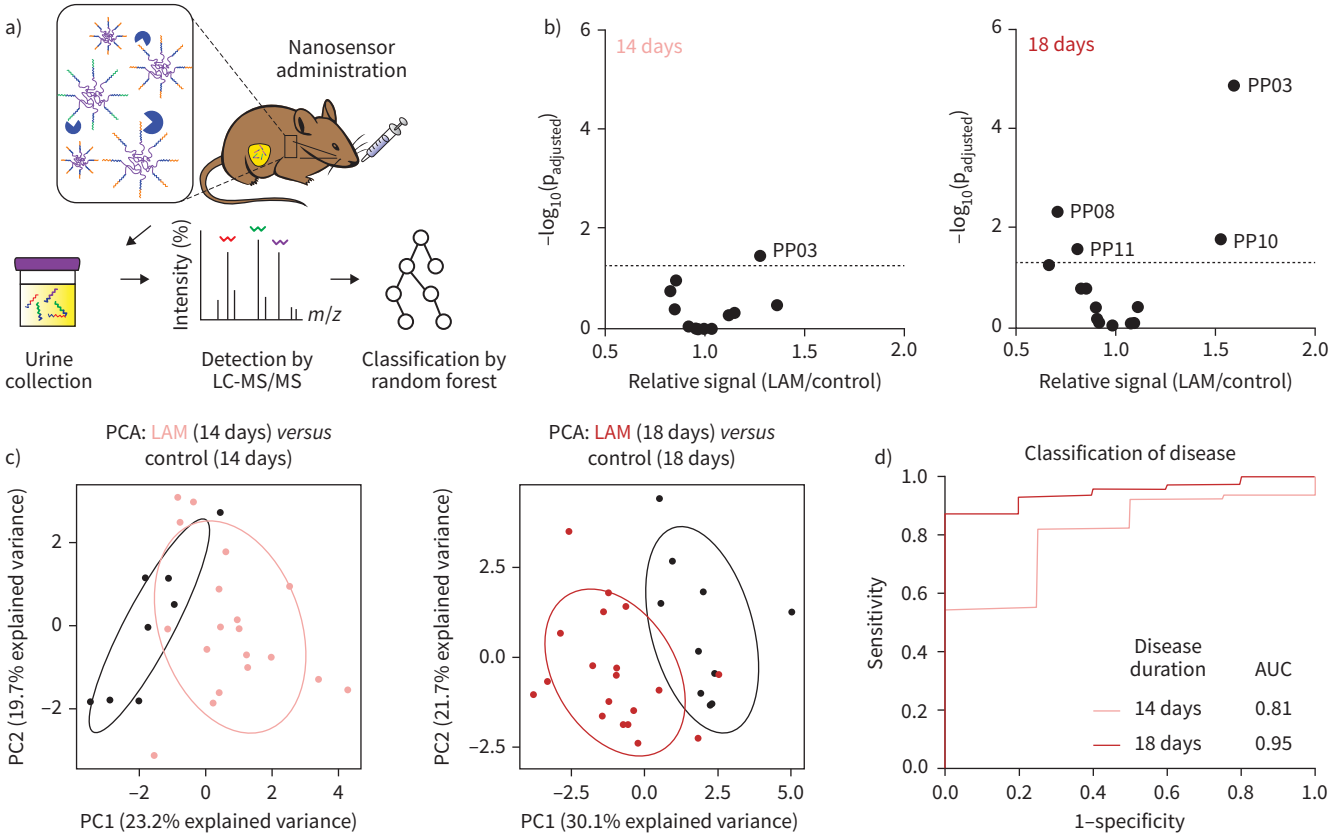

FIGURE 3 Activity-based nanosensors discriminate lymphangioleiomyomatosis (LAM) mice from healthy controls. a) Schematic of approach. b) Mean-scaled urinary reporter concentrations in LAM mice and healthy controls were compared at 14 days (LAM: n=19; control: n=9) and 18 days (LAM: n=19; control: n=10) after disease induction and $-\log_{10}(p_{adjusted})$ was plotted against fold change between LAM and control. Significance was calculated by the two-tailed t-test followed by adjustment for multiple hypotheses with Holm–Šídák correction. Dotted line is at $p_{adjusted}$=0.05. c) Principal component analysis (PCA) of urinary reporter output of LAM mice and healthy controls at 14 and 18 days after disease induction. d) A random forest classifier was trained on urinary reporters from a subset of LAM mice and healthy controls at both 14 days (LAM: n=5; control: n=5) and 18 days (LAM: n=5; control: n=5). Receiver operating characteristic curves show performance of this classifier in discriminating LAM mice from healthy controls in an independent test cohort at both 14 days (LAM: n=14; control: n=4) and 18 days (LAM: n=14; control: n=5) days. LC: liquid chromatography; MS: mass spectrometry; AUC: area under the curve.

altered by treatment with rapamycin, suggesting a profound shift in the pulmonary proteolytic landscape (figure 4b). Consistent with this finding, we found, by PCA, that LAM mice treated with rapamycin for 2 days clustered separately from both pre-treatment LAM mice and healthy controls (figure 4c and supplementary figure S12). However, continued rapamycin treatment for 8 days resulted in pulmonary protease activity that clustered closely with controls. Finally, we trained two random forest classifiers using a subset of LAM mice at day 18 and rapamycin-treated mice after 2 or 8 days of therapy, and tested their ability to accurately classify treated and untreated mice in an independent cohort. We found that the classifiers accurately distinguished treated and untreated mice at both tested time-points, with the strongest classification at 2 days after treatment induction (AUC 0.94) (figure 4d). Therefore, activity-based nanosensors rapidly and reliably detect response to rapamycin in a mouse model of pulmonary LAM.

Discussion

In this work, we demonstrate the utility of activity-based nanosensors for monitoring progression and treatment response in a novel pre-clinical model of pulmonary LAM. We found that a multiplexed panel of sensors enabled classification of disease, driven primarily by increased pulmonary protease activity against two sensors, PP03 and PP10. Furthermore, we found that this protease activity returned to baseline 2 days after treatment initiation, enabling near-perfect classification of treatment response.

Treatment response monitoring *via in vivo* measurements of protease activity offers several advantages over other surrogate end-points such as serum biomarkers, imaging and spirometry. In LAM, pulmonary

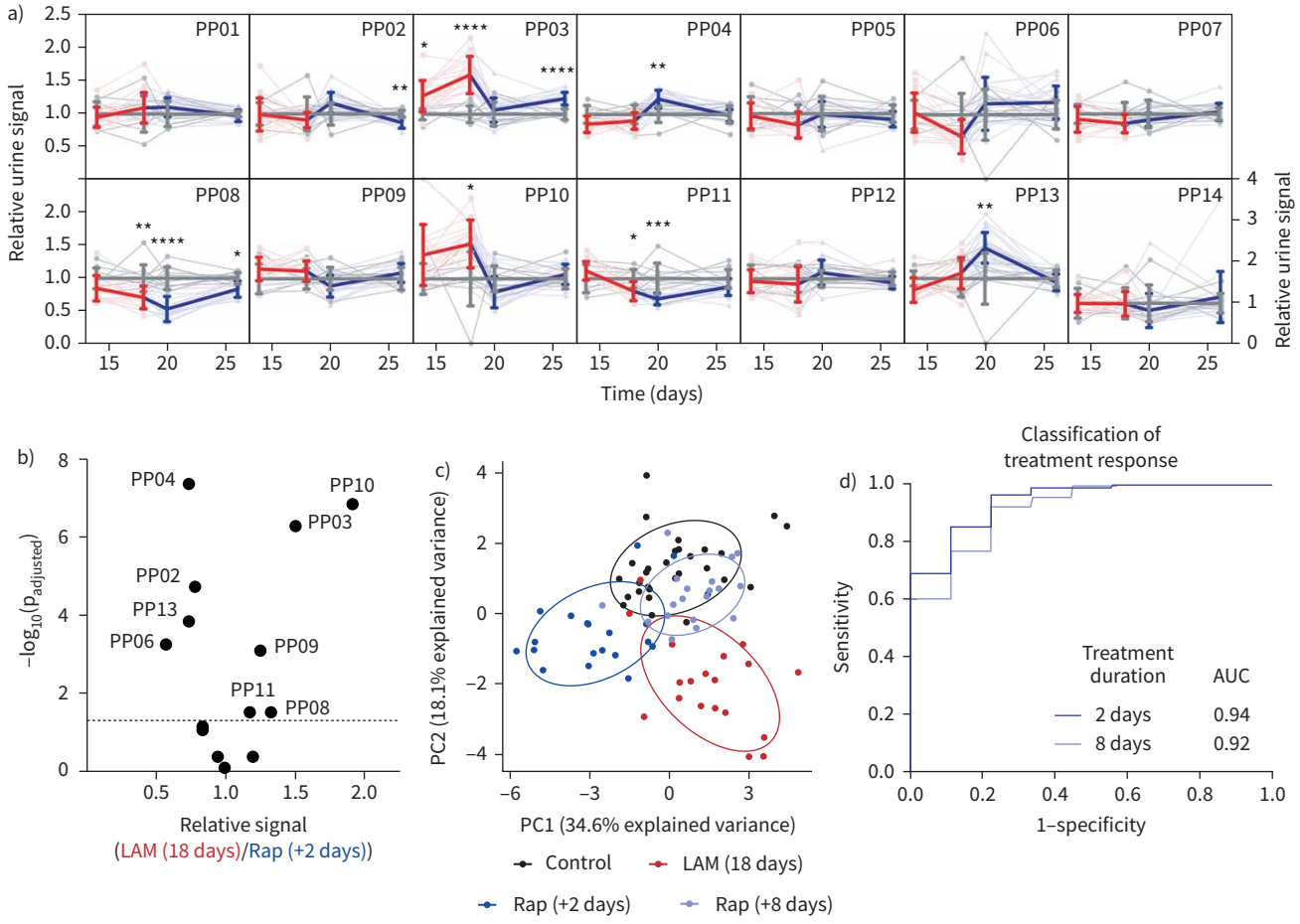

FIGURE 4 Activity-based nanosensors enable rapid assessment of drug response in lymphangioleiomyomatosis (LAM). a) Control-normalised urinary reporter signal for each of the 14 activity-based nanosensors PP01–PP14. Thin lines show activity-based nanosensor trajectories of each mouse over time, while thick lines are averages over all mice. Red lines represent LAM mice (n=19) prior to rapamycin treatment and blue lines represent LAM mice treated with 3 mg·kg^{-1} rapamycin (3–4 times per week). Grey lines represent healthy control mice (n=10). *: p<0.05; **: p<0.01; ***: p<0.001; ****: p<0.0001 from control. Error bars are SD. For clarity, PP14 is presented on a larger scale *y*-axis. b) Volcano plot showing the significance ($-\log_{10}(p_{adjusted})$) and fold change of each urinary reporter in LAM mice 18 days after 105K-Luc cell injection ("LAM (18 days)") relative to LAM mice after 2 days of rapamycin treatment ("Rap (+2 days)"). Dotted line is at $p_{adjusted}$=0.05. c) Mean-scaled urinary reporter concentrations were normalised to matched controls at each time-point and subjected to principal component analysis. d) Two random forest classifiers were trained on urinary reporters from a subset of LAM (18 days) mice (n=10) and either Rap (+2 days) (n=10) or Rap (+8 days) (n=10) mice. Receiver operating characteristic curves show performance of these classifiers in discriminating Rap (+2 days) (n=9) and Rap (+8 days) (n=9) mice from untreated LAM (18 days) (n=9) mice in independent, held-out test cohorts from the same experiment. AUC: area under the curve.

protease dysregulation may contribute directly to lung degradation, leading to pulmonary function decline and lung failure [1, 7, 8]. Therefore, measuring protease activity at the site of disease may offer the most direct means of assessing disease activity and predicting long-term outcomes. In contrast, biomarkers found in the blood are inherently correlative, as evidenced by the lack of concordance between changes in serum biomarker concentrations and long-term clinical outcomes in patients with LAM [16]. Although imaging methods such as HRCT enable direct visualisation of cyst volume, which correlates with pulmonary function, these findings do not appear to reverse in response to treatment [31]. Finally, pulmonary function testing is the gold standard method for determining pulmonary function, but its utility is limited in treatment response monitoring because of technical variability and long lag times [1]. Although a clinical study would be necessary to fully validate their utility in predicting long-term outcomes, activity-based nanosensors may offer the most direct and rapidly responsive method of reading out disease activity and treatment efficacy in LAM.

Our work also reveals new insights into the biology of disease progression and rapamycin response in our mouse model of LAM. Recent co-culture experiments have shown that extracellular acidification by

LAM-associated fibroblasts results in increased expression and activity of the lysosomal protease CTSK by *TSC2*$^{-/-}$ cells [28]. Intriguingly, PP03 and PP10, the two nanosensors that were preferentially cleaved in LAM mice, are the only sensors in the panel that are cleaved by the canonical lysosomal proteases NAPSA (figure 2e, supplementary figures S7 and S8 and supplementary table S1) and cathepsin D (CTSD) [21] under acidic conditions. In this work, we also demonstrated efficient cleavage of PP03 and PP10 by CTSK in acidic buffer. Finally, PP03 was the only peptide that was preferentially cleaved by 105K tumour homogenates under acidic conditions. These findings suggest that activity-based nanosensors may enable real-time monitoring of extracellular acidification and the resulting aberrations in protease activity in LAM. Notably, we found that treatment with rapamycin resulted in a rapid return to healthy levels for both PP03 and PP10, consistent with findings that rapamycin treatment inhibits extracellular acidification and protease activity *in vitro* [28]. The apparent decrease in serine protease activity, as evidenced by the negative correlation between disease burden and urinary PP08 and PP11 signal, may reflect an increase in the expression of serine protease inhibitors over the course of disease progression, a feature of other lung diseases [32, 33], but one that has yet to be described in LAM. Finally, we observed transiently increased cleavage of multiple nanosensors following rapamycin treatment. PP04, the sensor with the most significant increase in cleavage, is most efficiently cleaved *in vitro* by serine proteases, including those involved in the immune response [21]. Although further studies will be necessary to fully elucidate the mechanism underlying this transiently increased protease activity, our results highlight the power of activity-based nanosensors to directly query disease-relevant biological processes *in vivo*.

This work establishes activity-based nanosensors as a new paradigm for monitoring progression and treatment response in LAM, but future studies should address key limitations and unanswered questions. In particular, we did not fully characterise the mouse model described here for evidence of cystic lung destruction, lymphatic involvement or pulmonary function decline, all of which are hallmarks of LAM in humans [1]. Furthermore, although numerous studies have described dysregulation of metalloproteases [3, 4] and CTSK [28] in LAM, a definitive causative link to disease progression has yet to be established, and a small trial of the MMP inhibitor doxycycline failed to yield clinical benefit in LAM patients [34]. Although we demonstrate that pulmonary cleavage of activity-based nanosensors rapidly responds to treatment with rapamycin in mice, we did not assess whether these changes corresponded to long-term functional outcomes in our mouse model. Clinical trials will be necessary to assess the utility of activity-based nanosensors in predicting long-term response to therapy. Finally, we delivered activity-based nanosensors *via i.t.* instillation, but a clinically compatible delivery method such as dry powder inhalation or nebulisation will be required for use in humans.

In summary, we have demonstrated the utility of activity-based nanosensors in monitoring progression and treatment response in a mouse model of LAM. Clinically, activity-based nanosensors may enable rapid assessment of treatment response in patients treated with either rapamycin or emerging experimental therapies. By enabling real-time monitoring of disease activity, activity-based nanosensors may dramatically increase the pace of clinical trials and provide accurate and timely information to guide patient care.

Acknowledgements: We thank A.D. Warren and H.E. Fleming (Koch Institute for Integrative Cancer Research, MIT, Cambridge, MA, USA) for assisting with conceptualisation of the study and experimental design, and for critical editing of the manuscript, respectively; and A. Mancino (Syneos Health, Princeton, NJ, USA) for performing mass spectrometry; and the Koch Institute Swanson Biotechnology Center (MIT), specifically the Histology core and the Preclinical Modeling, Imaging and Testing core, for technical assistance.

Author contributions: J.D. Kirkpatrick, J.S. Dudani, E.P. Henske and S.N. Bhatia initiated the study. J.D. Kirkpatrick and A.P. Soleimany performed experiments and statistical analysis. J.D. Kirkpatrick, A.P. Soleimany, J.S. Dudani, H-J. Liu, H.C. Lam, C. Priolo, E.P. Henske and S.N. Bhatia contributed to experimental design and data interpretation. S.N. Bhatia and E.P. Henske supervised the research. J.D. Kirkpatrick and S.N. Bhatia wrote the first draft of the manuscript. All authors contributed to writing and editing subsequent drafts of the manuscript and approved the final manuscript.

Conflict of interest: J.D. Kirkpatrick reports grants from the Ludwig Fund for Cancer Research, during the conduct of the study. In addition, J.D. Kirkpatrick has a patent pending (Lung protease nanosensors and uses thereof; PCT/US2019/052868, filed 25 September 2019). A.P. Soleimany has nothing to disclose. J.S. Dudani has nothing to disclose. H-J. Liu has nothing to disclose. H.C. Lam has nothing to disclose. C. Priolo has nothing to disclose. E.P. Henske has nothing to disclose. S.N. Bhatia reports other support from the Howard Hughes Medical Institute and National Institute of Environmental Health Sciences, grants from the Ludwig Fund for Cancer Research and

grants from the Koch Institute Marble Center for Cancer Nanomedicine, during the conduct of the study; other support from Vertex Pharmaceuticals, Glympse Bio, Maverick Therapeutics, Satellite Bio, CEND Rx and Moderna Therapeutics, outside the submitted work. In addition, S.N. Bhatia has a patent pending (Lung protease nanosensors and uses thereof; PCT/US2019/052868, filed 25 September 2019).

Support statement: This study was supported in part by a Koch Institute Support Grant P30-CA14051 from the National Cancer Institute (Swanson Biotechnology Center), a Core Center Grant P30-ES002109 from the National Institute of Environmental Health Sciences, the Ludwig Fund for Cancer Research, and the Koch Institute Marble Center for Cancer Nanomedicine. J.D. Kirkpatrick acknowledges support from a Ludwig Center Fellowship. A.P. Soleimany acknowledges support from a National Institutes of Health Molecular Biophysics Training Grant (NIH/NIGMS T32 GM008313) and National Science Foundation Graduate Research Fellowship. J.S. Dudani acknowledges support from a National Science Foundation Graduate Research Fellowship, a Ludwig Center Fellowship and the Siebel Scholar Foundation. S.N. Bhatia is a Howard Hughes Medical Institute Investigator. Funding information for this article has been deposited with the Crossref Funder Registry.

References

1 Henske EP, McCormack FX. Lymphangioleiomyomatosis – a wolf in sheep's clothing. *J Clin Invest* 2012; 122: 3807–3816.
2 Guo M, Yu JJ, Perl AK, *et al.* Single cell transcriptomic analysis identifies a unique pulmonary lymphangioleiomyomatosis cell. *Am J Respir Crit Care Med* 2020; 202: 1373–1387.
3 Hayashi T, Fleming MV, Stetler-Stevenson WG, *et al.* Immunohistochemical study of matrix metalloproteinases (MMPs) and their tissue inhibitors (TIMPs) in pulmonary lymphangioleiomyomatosis (LAM). *Hum Pathol* 1997; 28: 1071–1078.
4 Matsui K, Takeda K, Yu ZX, *et al.* Role for activation of matrix metalloproteinases in the pathogenesis of pulmonary lymphangioleiomyomatosis. *Arch Pathol Lab Med* 2000; 124: 267–275.
5 Lee PS, Tsang SW, Moses MA, *et al.* Rapamycin-insensitive up-regulation of MMP2 and other genes in tuberous sclerosis complex 2-deficient lymphangioleiomyomatosis-like cells. *Am J Respir Cell Mol Biol* 2010; 42: 227–234.
6 Zhu L, Tang Y, Li X, *et al.* Osteoclast-mediated bone resorption is controlled by a compensatory network of secreted and membrane-tethered metalloproteinases. *Sci Transl Med* 2020; 12: eaaw6143.
7 Babaei-Jadidi R, Dongre A, Miller S, *et al.* Mast-cell tryptase release contributes to disease progression in lymphangioleiomyomatosis. *Am J Respir Crit Care Med* 2021; 204: 431–444.
8 Moses MA, Harper J, Folkman J. Doxycycline treatment for lymphangioleiomyomatosis with urinary monitoring for MMPs. *N Engl J Med* 2006; 354: 2621–2622.
9 Goncharova EA, Goncharov DA, Fehrenbach M, *et al.* Prevention of alveolar destruction and airspace enlargement in a mouse model of pulmonary lymphangioleiomyomatosis (LAM). *Sci Transl Med* 2012; 4: 154ra134.
10 Bissler JJ, McCormack FX, Young LR, *et al.* Sirolimus for angiomyolipoma in tuberous sclerosis complex or lymphangioleiomyomatosis. *N Engl J Med* 2008; 358: 140–151.
11 McCormack FX, Inoue Y, Moss J, *et al.* Efficacy and safety of sirolimus in lymphangioleiomyomatosis. *N Engl J Med* 2011; 364: 1595–1606.
12 McCormack FX, Gupta N, Finlay GR, *et al.* Official American Thoracic Society/Japanese Respiratory Society clinical practice guidelines: lymphangioleiomyomatosis diagnosis and management. *Am J Respir Crit Care Med* 2016; 194: 748–761.
13 Johnson SR, Cordier JF, Lazor R, *et al.* European Respiratory Society guidelines for the diagnosis and management of lymphangioleiomyomatosis. *Eur Respir J* 2010; 35: 14–26.
14 Krowka MJ, Enright PL, Rodarte JR, *et al.* Effect of effort on measurement of forced expiratory volume in one second. *Am Rev Respir Dis* 1987; 136: 829–833.
15 Nijmeh J, El-Chemaly S, Henske EP. Emerging biomarkers of lymphangioleiomyomatosis. *Expert Rev Respir Med* 2018; 12: 95–102.
16 Young LR, Lee HS, Inoue Y, *et al.* Serum VEGF-D concentration as a biomarker of lymphangioleiomyomatosis severity and treatment response: a prospective analysis of the Multicenter International Lymphangioleiomyomatosis Efficacy of Sirolimus (MILES) trial. *Lancet Respir Med* 2013; 1: 445–452.
17 Young LR, VanDyke R, Gulleman PM, *et al.* Serum vascular endothelial growth factor-D prospectively distinguishes lymphangioleiomyomatosis from other diseases. *Chest* 2010; 138: 674–681.
18 Lamattina AM, Taveira-Dasilva A, Goldberg HJ, *et al.* Circulating biomarkers from the phase 1 trial of sirolimus and autophagy inhibition for patients with lymphangioleiomyomatosis. *Chest* 2018; 154: 1070–1082.
19 Yao J, Taveira-DaSilva AM, Jones AM, *et al.* Sustained effects of sirolimus on lung function and cystic lung lesions in lymphangioleiomyomatosis. *Am J Respir Crit Care Med* 2014; 190: 1273–1282.
20 Kwong GA, von Maltzahn G, Murugappan G, *et al.* Mass-encoded synthetic biomarkers for multiplexed urinary monitoring of disease. *Nat Biotechnol* 2013; 31: 63–70.

21 Kirkpatrick JD, Warren AD, Soleimany AP, *et al.* Urinary detection of lung cancer in mice via noninvasive pulmonary protease profiling. *Sci Transl Med* 2020; 12: 262.

22 Dudani JS, Ibrahim M, Kirkpatrick J, *et al.* Classification of prostate cancer using a protease activity nanosensor library. *Proc Natl Acad Sci USA* 2018; 115: 8954–8959.

23 Loynachan CN, Soleimany AP, Dudani JS, *et al.* Renal clearable catalytic gold nanoclusters for *in vivo* disease monitoring. *Nat Nanotechnol* 2019; 14: 883–890.

24 Soleimany AP, Kirkpatrick JD, Su S, *et al.* Activatable zymography probes enable *in situ* localization of protease dysregulation in cancer. *Cancer Res* 2021; 81: 213–224.

25 Soleimany AP, Bhatia SN. Activity-based diagnostics: an emerging paradigm for disease detection and monitoring. *Trends Mol Med* 2020; 26: 450–468.

26 Soleimany AP, Kirkpatrick JD, Wang CS, *et al.* Multiscale profiling of enzyme activity in cancer. *bioRxiv* 2021; preprint [https://doi.org/10.1101/2021.11.11.468288].

27 Parkhitko AA, Priolo C, Coloff JL, *et al.* Autophagy-dependent metabolic reprogramming sensitizes TSC2-deficient cells to the antimetabolite 6-aminonicotinamide. *Mol Cancer Res* 2014; 12: 48–57.

28 Dongre A, Clements D, Fisher AJ, *et al.* LAM cell–fibroblast interactions enhance protease activity by extracellular acidification. *Am J Pathol* 2017; 187: 1750–1762.

29 Bossard MJ, Tomaszek TA, Thompson SK, *et al.* Proteolytic activity of human osteoclast cathepsin K: expression, purification, activation, and substrate identification. *J Biol Chem* 1996; 271: 12517–12524.

30 Crino PB, Nathanson KL, Henske EP. The tuberous sclerosis complex. *N Engl J Med* 2006; 28: 1345–1356.

31 Gopalakrishnan V, Yao J, Steagall WK, *et al.* Use of CT imaging to quantify progression and response to treatment in lymphangioleiomyomatosis. *Chest* 2019; 155: 962–971.

32 Vignola AM, Bonanno A, Mirabella A, *et al.* Increased levels of elastase and α_1-antitrypsin in sputum of asthmatic patients. *Am J Respir Crit Care Med* 1998; 157: 505–511.

33 Betsuyaku T, Takeyabu K, Tanino M, *et al.* Role of secretory leukocyte protease inhibitor in the development of subclinical emphysema. *Eur Respir J* 2002; 19: 1051–1057.

34 Chang WYC, Cane JL, Kumaran M, *et al.* A 2-year randomised placebo-controlled trial of doxycycline for lymphangioleiomyomatosis. *Eur Respir J* 2014; 43: 1114–1123.